



Establishing a Design Strategy for Corrosion Resistant Structural Materials in Molten Salt Technologies

R. PILLAI,^{1,3} D. SULEJMANOVIC,¹ T. LOWE,¹ S.S. RAIMAN,²
and B.A. PINT¹

1.—Materials Science and Technology Division, Oak Ridge National Laboratory, Oak Ridge, TN 37831-6156, USA. 2.—College of Engineering, Nuclear Engineering and Radiological Sciences, University of Michigan, Ann Arbor, MI 48109-2104, USA. 3.—e-mail: pillairr@ornl.gov

To address the gap in material design strategies for structural components in molten salt-powered technologies, the current work aimed to identify key parameters governing corrosion induced degradation of materials during exposures in molten halide salts. The applicability of the data on dissolution rates of pure metals (e.g., Cr) in a given molten salt to enable predictions of corrosion behavior of multicomponent binary and ternary Fe-based model and Ni-based commercial alloys isothermally exposed in the purified KCl-MgCl₂ in quartz capsules at 700 and 800 °C was evaluated. The influence of alloy chemistry on initial dissolution rates and the consequent impact on the time-dependent corrosion induced microstructural evolution in the alloy subsurface was predicted with a coupled thermodynamic-kinetic model. The model was well able to predict the Cr depletion in all investigated alloys demonstrating the ability of the proposed approach to enable a unique design strategy for structural materials in molten salts.

INTRODUCTION

Molten salt reactor (MSR) concepts present a promising path toward advancing the role of nuclear energy in the envisioned carbon-neutral power generation portfolio.^{1,2} The attractive properties of molten halide salts such as low vapor pressure, strong negative temperature coefficient of reactivity and minimal heat generation by radioactive decay advocate for the construction of new MSRs since they ensure clean, safe and economical

This manuscript has been authored by UT-Battelle, LLC, under contract DE-AC05-00OR22725 with the US Department of Energy (DOE). The US government retains and the publisher, by accepting the article for publication, acknowledges that the US government retains a nonexclusive, paid-up, irrevocable, worldwide license to publish or reproduce the published form of this manuscript, or allow others to do so, for US government purposes. DOE will provide public access to these results of federally sponsored research in accordance with the DOE Public Access Plan (<http://energy.gov/downloads/doe-public-access-plan>).

(Received June 7, 2022; accepted November 30, 2022;
published online January 3, 2023)

energy.^{3–5} Furthermore, MSRs may also benefit from exploring opportunities beyond power generation and probe their potential in chemical synthesis processes by enabling production of alternative fuels such as hydrogen.⁶ This will require an increase in reactor temperatures since production of hydrogen demands operating temperatures in the range of 800–1000 °C.⁶ Although there is extensive experimental work with operation of various MSR concepts and structural materials for operation at temperatures between 650–700 °C,^{7,8} there is limited information on the compatibility of candidate structural materials at higher temperatures.⁹ The Ni-base alloy Inconel (Ni-15Cr-7Fe-Al0.15-Ti0.25-Si-0.22-Mn0.03C-0.04-0.06 wt.%) exposed in the NaF-ZrF₄-UF₄ salt during the aircraft reactor experiment at 816 °C (molten salt temperature) showed a significant depth of attack of about 200 μm after 500 h and 450 μm after 3000 h. Furthermore, recent studies have shown considerable corrosion rates of materials such as stainless steels and certain Ni-base alloys at these temperatures in molten salts with major influencing factors being salt and alloy composition, interaction with

container material and impurities in the salts (O_2 and H_2O).^{10–13} Existing impurities in the salts such as H_2O , NiF_2 , $NiCl_2$, FeF_2 , $FeCl_2$ or contamination due to leakages in the system would tend to accelerate these reactions by forming HF/HCl through reactions with the salt. Operation at higher temperatures presents an even bigger challenge, and extensive experimental efforts to evaluate materials compatibility are expensive and retard the development process.

During exposure of a structural material in molten halide salts, multiple corrosion mechanisms such as galvanic corrosion, anodic dissolution, impurity driven corrosion and thermal gradients might be simultaneously active.^{14–17} Despite the long history of research on the molten-salt corrosion of structural materials, there are significant gaps in our scientific understanding of the governing mechanisms primarily due to the complexity of isolating the effects of each of the aforementioned mechanisms.¹⁸ Experimental evaluations under realistic test conditions are essential to evaluate compatibility of the candidate materials during exposures in molten salts. However, an extensive test matrix might be needed to investigate the influence of different salt chemistries and alloy compositions as a function of time and temperature. High-fidelity physics-based models with the ability to capture the underlying material degradation processes and predict material behavior as a function of salt chemistry, alloy composition, time and temperature can significantly reduce the experimental effort and simultaneously improve the mechanistic understanding.

Modeling efforts in the literature are either primarily limited to surface reactions^{19,20} or do not consider chemical interactions of alloying elements in a multicomponent alloy system and thereby ignore altered driving forces for species transport during corrosion on the surface.^{21–23} In an earlier work,¹⁸ the authors of the present study presented an initial attempt to address this gap by evaluating the applicability of a coupled thermodynamic-kinetic modeling approach in describing the role of the capsule material and alloy composition of model and commercial Ni-based alloys on the observed corrosion rates during exposure in high-purity binary and commercial $KCl-MgCl_2$ salts at 600 °C–800 °C in Mo and Ni capsules. Thermodynamic and kinetic calculations showed that Cr activity in the alloy rather than its concentration is a more relevant parameter governing corrosion behavior in molten halide salts. Recent studies have provided further evidence for this hypothesis by showing the predominant role of chemical activities rather than galvanic effects in governing mass transport between dissimilar materials exposed in molten fluoride salts.^{24,25} Furthermore, the simultaneous dissolution of Fe, Cr and Mn was observed from the Ni-based alloys reemphasizing the need to integrate the role of alloy chemistry in such modeling efforts.

The present work aims to verify the previously proposed¹⁸ degradation mechanisms and thereby the rate-limiting driving forces for corrosion of Fe- and Ni-based alloys in molten halide salts. Model binary, ternary and quaternary Fe-based and multicomponent commercial Ni-based alloys were exposed in the binary eutectic $KCl-MgCl_2$ chloride salt at 700 °C and 800 °C in quartz capsules for 100 h. The dissolution rates of Cr from the alloys were estimated from previously measured²⁶ corrosion rates of pure Cr in the same salt. Cr depletion from the alloys was calculated with the coupled thermodynamic-kinetic model²⁷ and compared with measured depletion profiles in the alloys and correlated to the measured Cr content of the salts after exposure.

EXPERIMENTAL PROCEDURE

Materials and High-Temperature Molten Salt Exposures

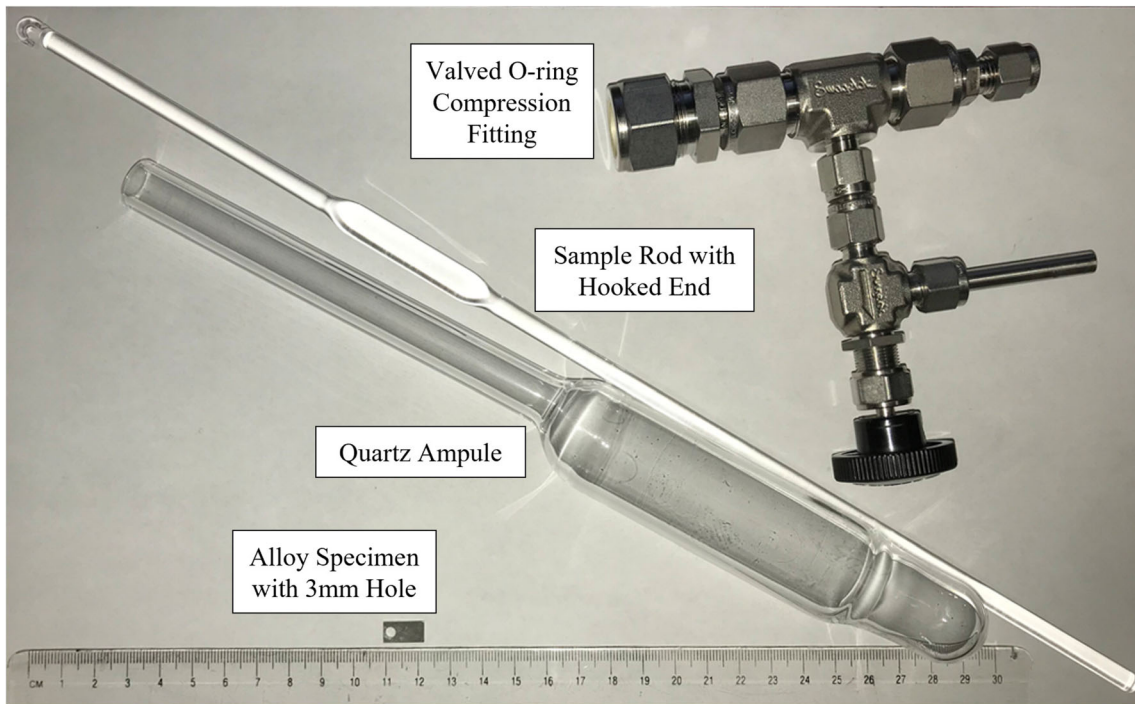
The chemical composition of the studied alloys is given in Table I. The model alloys were vacuum-induction melted and solidified in water-cooled copper molds. Average grain sizes of the binary Fe-Cr alloys were about 800–1000 μm and were significantly smaller (25–40 μm) for the ternary Fe-Cr-Ni model alloys. Isothermal static capsule testing was conducted in quartz capsules (25 mm outer diameter \times 76 mm tall \times 1.2 mm wall). To achieve a salt volume to specimen surface area ratio > 10 , small rectangular coupons (12 \times 5 \times 0.5–1.5 mm) were used and polished to 600 grit finish before exposure.

A binary $KCl-MgCl_2$ eutectic (68:32 mol%) salt mixture was employed for corrosion testing. The salt was purified, primarily to eliminate O_2 and H_2O impurities, using a two-step process previously described here.^{28,29} The first step involved mixing the salt with NH_4Cl (2:1) followed by heating to 450 °C for 2 h and 750 °C for 1 h. This was followed by sparging at 850 °C first with CCl_4 for 35–40 h, then with ultra-high purity (UHP: 99.999% purity) Ar for 0.5 h followed by Ar–4% H_2O for 12–15 h and finally with UHP Ar for 0.5 h.

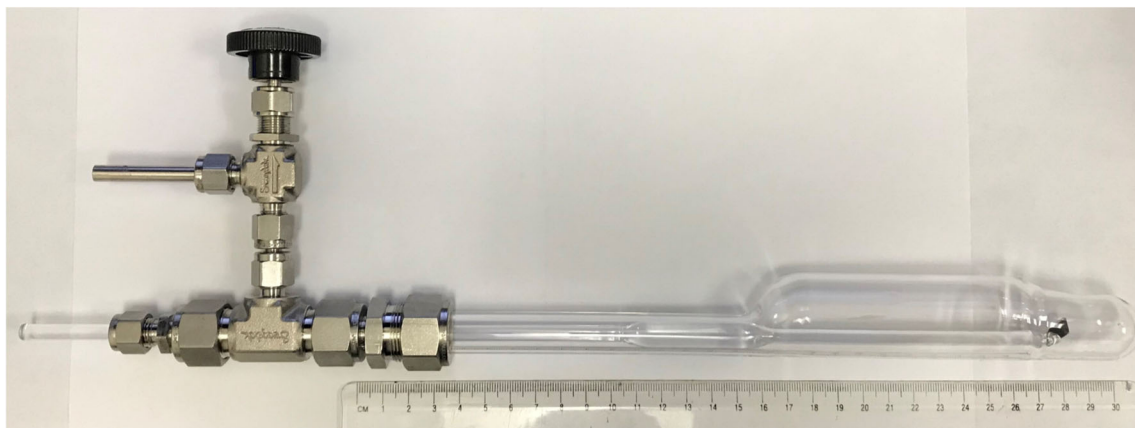
Quartz was chosen as capsule material based on previous experience (unpublished work), which showed the inert nature of quartz in these salts under these test conditions. Quartz ampules were loaded with 28 g of salt in an Ar-filled glove box with impurity levels < 1 ppm O_2 and H_2O . The coupons were taken into an inert glove box to load into the corrosion vessel. Quartz ampules were cleaned by filling with KOH in isopropanol overnight. The tubes were emptied, thoroughly rinsed with 18.2 M Ω -cm water and dried in an oven at 120 °C for 2 h. The tubes were taken into the glove box while hot to load for the corrosion experiment. Images of the capsule design are given in Fig. 1. The sealed capsules containing the specimens were isothermally exposed in a box furnace in laboratory air at 700 °C and 800 °C for 100 h. After the isothermal exposure, the capsules were cooled and

Table I. Composition of studied model and commercial alloys (in wt%) analyzed by inductively coupled plasma-optical emission spectrometry (ICP-OES) and combustion analysis for carbon

Composition	Ni	Cr	Fe	Mo	Mn	Si	Al	Ti	W	Co	V	Nb	C
Fe-15Cr	–	14.9	Bal.	–	–	–	–	–	–	–	–	–	–
Fe-20Cr	–	19.9	Bal.	–	–	–	–	–	–	–	–	–	–
Fe-30Cr	–	30.4	Bal.	–	–	–	–	–	–	–	–	–	–
Fe-15Cr-Mn-Si	–	14.9	Bal.	–	0.6	0.3	–	–	–	–	–	–	–
Fe-20Cr-20Ni	20.5	20.1	Bal.	–	–	–	–	–	–	–	–	–	–
Fe-20Cr-30Ni	30.1	19.8	Bal.	–	–	–	–	–	–	–	–	–	–
740H	49.3	24.6	1.1	0.5	0.3	0.3	1.3	1.5	–	19.6	–	1.3	0.03
Haynes 230	60.3	21.8	0.74	1.2	0.44	0.17	0.37	0.005	14.6	0.053	–	–	0.09



(a)



(b)

Fig. 1. (a) Different components of the quartz ampule setup locations and (b) assembled quartz ampule with test specimen.

opened in the same glove box. To allow for the potential analyses of corrosion deposits, the specimens were not cleaned with water; consequently, no mass change was measured.

Static Tests in Mo capsules

The dissolution rates of Cr in the KCl-MgCl₂ salt mixture were previously measured by exposing pure Cr (99.99%) specimens in the salt.²⁶ The experimental procedure for these tests is briefly described here for clarity. For these static exposures in Mo capsules; specimens measuring approximately 1.8 × 12 × 20 mm were cut, polished to 600-grit finish and weighed to 0.04 mg accuracy using a Mettler Toledo model XP205 balance. Low current arc cast (LCAC) molybdenum capsules measuring 1 inch in diameter and 3 inches in length were cleaned using acid etching, and specimens were attached with molybdenum wire to one endcap of each capsule into which 30 g of the purified KCl-MgCl₂ eutectic (68:32 mol%) salt mixture was filled in an Ar glovebox. While still in the glovebox, the capsules were welded shut to create an air-tight seal. The molybdenum inner capsules were sealed within stainless steel outer capsules under Ar or vacuum for safety and secondary containment before heating in a box furnace for a maximum exposure time of 2000 h at 700 °C and 4630 h at 800 °C. Specimens were taken out after 100 h, 1000 h and 2000 h at 700 °C and after 522 h, 1625 h, 3217 h, 3625 h and 4630 h at 800 °C to measure mass change and analyze the salt chemistry.

Microstructural and Chemical Analyses

Post-exposure, specimens were Cu-plated and cross-sectioned for metallographic analyses. The mounted samples were ground to 1200 grit with SiC grinding papers and subsequently polished with diamond pastes to 1 μm surface finish. Water-free handling of the specimens was used to maximize the possibility of retaining the corrosion products. Microstructural characterization to measure compositional changes and identify corrosion products and phase transformations was performed using scanning electron (SE), back-scattered electron (BSE) microscopy (TESCAN MIRA3 SEM) and energy dispersive x-ray spectroscopy (EDS:EDAX Octane Elect Super Silicon Drift Detector).

The chemical compositions of the salts before and after high temperature exposure were measured with inductively coupled plasma atomic emission spectrometry (ICP-AES). Chloride concentration was measured by ion chromatography. The composition of the purified binary KCl-MgCl₂ before exposure was 23.4% K-10.9% Mg-Bal. chloride (wt%)

MODELING PROCEDURE

Homogenization Model

The simultaneously occurring corrosion, diffusion and dissolution processes in the alloys were modeled

in the present work with a coupled thermodynamic-kinetic approach to modeling based on the homogenization model presented by Larsson et al.³⁰ The model has been successfully applied to describe oxidation-induced material degradation for uncoated Ni-base alloys^{31–33} and coated Ni-base superalloys.^{27,34–37} A detailed description of the model can be found elsewhere.^{27,34} However, the modeling procedure will be briefly described with the governing flux equation.

The procedure begins with the discretization of the domain into a suitable number of volume elements or slices of width Δz^i , i being the slice number. The position of the boundaries of these slices is marked as z^j , where $j = i + 1$. The center of the slices is marked as z^i . Average mole fractions N_c^{i0} for each constituent c are assigned to each slice based on the initial composition of the system. Constant molar volume V_m is assumed across the entire specimen. In the first step, the phase fractions f_ϕ , compositions and chemical potentials μ_c^i in each slice are defined by the equilibrium resulting because of local element concentrations, temperature and pressure, e.g., in one volume element. The second step involves the choice of a suitable time step Δt for calculating diffusion of elements with the modified flux equation of Larsson et al.³⁸ in the lattice-fixed frame of reference. Efficient equilibration of vacancies ($\Delta\mu_{V_A} = 0$) was assumed. The flux of each constituent in a slice, $J_c^{i,j}$, is evaluated as follows,

$$J_c^{i,j} = -\frac{M_c^{i,\text{eff}} RT}{V_m(l^{i+1} - l^i)} \sqrt{N_c^{i+1} N_c^i} 2\sinh\left(\frac{\mu_c^{i+1} - \mu_c^i}{2RT}\right), \quad (1)$$

where $M_c^{i,\text{eff}}$ is the effective mobility of constituent c in slice i , μ_c^i is the chemical potential of constituent c at location i , R is the universal gas constant, and T is the temperature. Various homogenization rules to evaluate the local effective kinetic properties such as mobilities are documented in Ref. 30. In this work the upper Wiener bounds, more generally termed the “rule of mixtures,” has been used, and the commercially available thermodynamic databases TCFE11³⁹ (for Fe-based alloys) and TCNI11⁴⁰ (for Ni-based alloys) were used to calculate thermodynamic equilibria. To account for the grain-boundary assisted diffusion, the alloy constituent mobilities M_c extracted from the mobility database (MOBNI5⁴¹) were modified to M_c^{mod} in the following manner:

$$M_c^{\text{mod}} = \frac{\delta}{d} M_c^{\text{GB}} + \left(1 - \frac{\delta}{d}\right) M_c \quad (2)$$

where M_c^{GB} is the mobility of constituent c in grain boundaries, δ is the grain boundary width, and d is the grain size.

All the relevant phases α -ferrite (disordered BCC), γ (disordered FCC), γ' (ordered FCC), MC-type carbides and μ phase] were considered for calculations. Diffusion data for the alloying elements, assuming diffusion to occur only in the α -ferrite (disordered BCC) and γ (disordered FCC) phases, were extracted from the mobility databases MOBFE6⁴² and MOBN15,⁴¹ respectively.

Numerical Parameters

A geometric mesh was generated with a finer mesh at the alloy surface (left boundary) and gradually increasing cell size toward the specimen center (right boundary). The mesh was adapted at each time step since the domain would shrink because of corrosion-induced loss of Cr to the base alloy. The mesh adaption procedure was explained in an earlier work.²⁷

The corrosion-induced Cr loss was employed as a boundary condition on the alloy surface. The Cr loss kinetics for the investigated alloys were derived from previously measured²⁶ dissolution rates of pure Cr in the KCl-MgCl₂ eutectic (68:32 mol%) salt mixture. This is in line with DeVan's work¹⁴ where he measured the equilibrium concentration of the Cr ions in the LiF-KF-NaF-UF₄ salt after exposure of pure Cr at 600 °C and 800 °C. DeVan proposed that under the conditions of pure Cr ($a_{Cr}=1$) in equilibrium with the fluoride salt, the mole fraction of Cr (N_{Cr}), driven by its reaction with UF₄, measured in the salt, can be considered equivalent to the mole fractions of N_{CrF_2} and N_{CrF_3} . Based on an additional assumption about the small change in the salt concentration of UF₄, N_{Cr} was calculated to be proportional to the Cr activity in the alloy. DeVan achieved acceptable agreement between the measured Cr concentration in the salt and the predicted Cr loss from the alloy after 500 h and 1000 h, which were shown to correspond to equilibrium concentrations.

Using a similar approach in which Cr reacts with the salt to form CrCl₂, the equilibrium constant for the formation of CrCl₂ can then be formulated with the activities of CrCl₂ (a_{CrCl_2}), Cr (a_{Cr}) and partial pressure of Cl₂ equivalent to the redox potential (p_{Cl_2}) as follows,

$$K = \frac{a_{CrCl_2}}{a_{Cr}p_{Cl_2}} \quad (3)$$

Further assuming that the concentrations of CrCl₂ are relatively low, Eq. 3 can be reformulated with its respective mole fractions based on Henry's law as follows,

$$K = \frac{N_{CrCl_2}}{a_{Cr}p_{Cl_2}} \quad (4)$$

Considering $N_{Cr} = N_{CrCl_2}$, a similar formulation as in Eq. 4 can be written for the mole fraction of Cr lost from the alloy $N_{Cr,alloy}$ and the corresponding Cr

activity in the alloy $a_{Cr,alloy}$. The Cr loss from the alloy at equilibrium can then be scaled as follows with $a_{Cr}=1$ for pure Cr,

$$N_{Cr,alloy} = N_{Cr}a_{Cr,alloy}. \quad (5)$$

The modeling approach presented here assumes local equilibrium at the salt-alloy interface based on the Cr from the alloy reacting with the salt to form CrCl₂. This local equilibrium will continue to be maintained as long as the assumed compound is being formed based on the local Cl potential. However, the rate of formation of this compound will be governed by the surface Cr activity, and this is what Eq. 5 describes. The depletion of Cr from the alloy will be governed by the chemical potential gradient from the surface to the bulk. Consequently, Cr will continue to be depleted from the alloy as long as this gradient can be sustained.

The amount of Cr lost from the pure Cr specimens was derived from the measured area-specific mass change²⁶ and total amount of salt (28 g) in the capsule. The squared Cr loss values are plotted against time in Fig. 2a. The Cr loss kinetics were fitted ($R^2 > 0.95$) to a power time law of the type $N_{Cr} = (k_{Cr}t)^n$ where n is the exponent ($n = 0.5$). The measured Cr loss after 1000 h at 700 °C was similar to the exposure after 100 h. The precise reason for this could not be identified, and this point was not considered to estimate the time dependence of the Cr loss. The Cr dissolution rate $k_{Cr,alloy}$ for an alloy can then be derived with Eq. 5 and corresponding chemical activity of Cr in the alloy.

The assumption of symmetry at the center of the sample provided the second spatial boundary condition (specimen center) of zero flux for all elements on the other side of the domain. The measured compositions of the alloy in the as-received state (Table I and Fig. 1) was used as the initial composition at time $t = 0$. The model provided average element concentrations and phase fractions as a function of time and distance.

RESULTS AND DISCUSSION

Model Alloys

The calculated chemical activities of Cr (with BCC as reference state for Cr) in each of the investigated alloys at 700 °C and 800 °C are given in Fig. 2b. Generally, Cr activity is predicted to increase with increasing Cr concentrations in the alloys but there are some key differences to point out, which are expected to influence the corrosion behavior of these alloys, as will be discussed in the following sections. The Cr activity in the ternary Fe-Cr-Ni model alloys is higher than the binary Fe-20Cr alloy with a similar Cr content at both temperatures.

Figure 3 compares the measured and calculated Cr depletion profiles in Fe-15Cr, Fe-20Cr and Fe-30Cr after exposure for 100 h in the binary KCl-

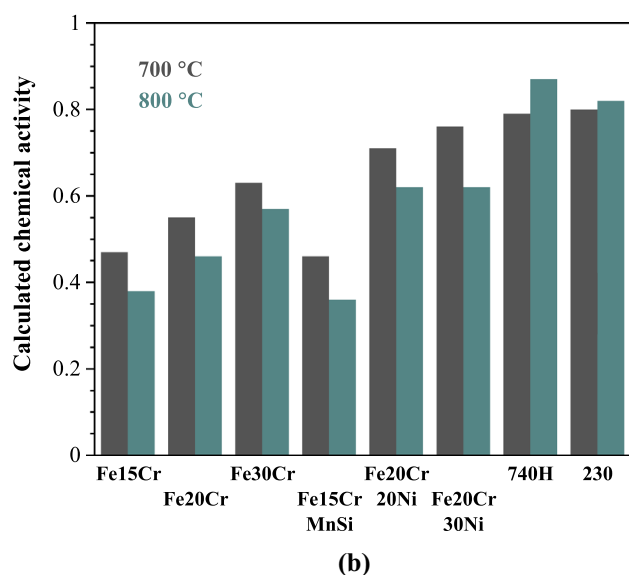
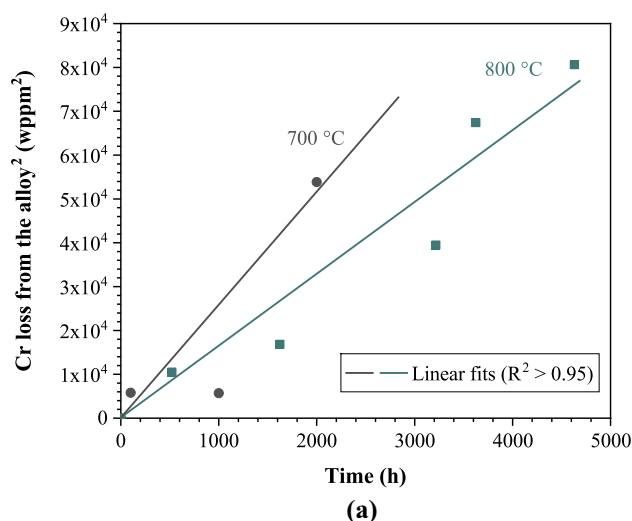


Fig. 2. (a) Cr loss derived from measured mass change after exposure of pure Cr in the binary KCl-Mg₂Cl₂ eutectic (68:32 mol%) salt mixture at 700 °C and 800 °C, (b) Cr activity for the investigated alloys at 700 °C and 800 °C calculated (thermodynamic database TCNI11) with BCC as reference state for Cr and the measured compositions in Table 1.

MgCl₂ eutectic (68:32 mol%) salt mixture at 700 °C and 800 °C. The excellent agreement between the two quantities supports the hypothesis that Cr dissolution rates are directly proportional to the corresponding Cr activities in the alloy. Figure 2b shows that the minor additions of Mn and Si do not significantly impact the Cr activity of the alloy and should not thereby influence the Cr dissolution rate. Figure 4 compares the measured and calculated Cr depletion profiles in the Fe-15Cr and Fe-15Cr-0.6Mn-0.25Si model alloys. Almost identical depletion profiles provide additional evidence for the hypothesis presented in this work. The corresponding calculated Cr depletion profile in Fe-15Cr-0.6Mn-0.25Si is plotted for comparison and agrees well with the measured Cr concentration profile.

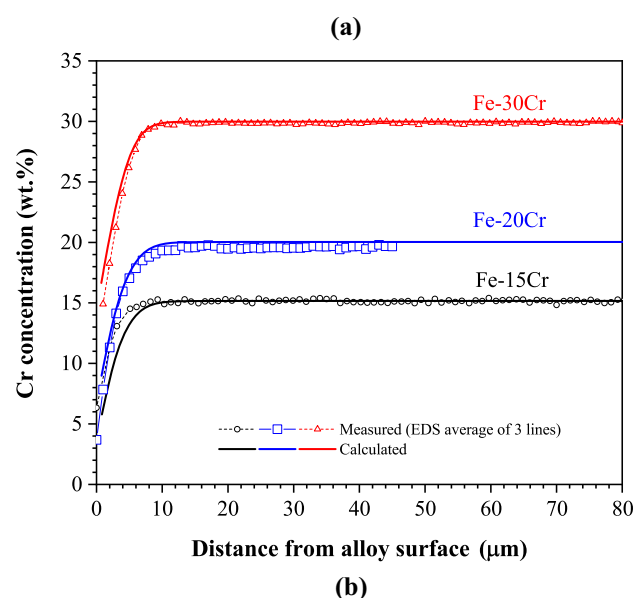
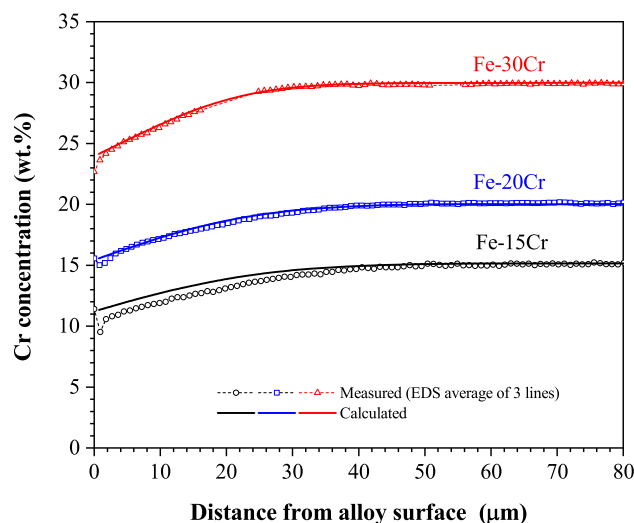


Fig. 3. Comparison between the measured (EDS) and calculated Cr depletion profiles in Fe-15Cr, Fe-20Cr and Fe-30Cr after exposure for 100 h in the binary KCl-Mg₂Cl₂ eutectic (68:32 mol%) salt mixture at (a) 700 °C and (b) 800 °C. The symbols correspond to the average Cr concentrations calculated from three measured concentration profiles across the specimen. No significant variation was observed between these measurements, and the error bars spanning the minimum and maximum measured Cr concentrations from these measurements have been omitted for better readability. The solid line corresponds to the calculated Cr depletion profiles.

The considerably smaller grain size (20–40 µm) of the austenitic model alloys Fe-20Cr-20Ni and Fe-20Cr-30Ni changes the mode of attack from a frontal type in the binary Fe-Cr alloys to the grain boundaries. This is demonstrated in the Cr distribution maps (EDS) shown in Fig. 5 for the two alloys. This is primarily due to the slower diffusion of Cr in the austenitic matrix at these temperatures,⁴³ and Cr depletion can be expected to occur mainly via grain boundary transport. The grain boundary mobility (Eq. 2) was estimated by halving the activation energy for volume diffusion. It is well

established that the grain boundary activation energy in pure metals is nearly half of the value for volume diffusion.⁴⁴ This is not necessarily true for multicomponent alloys because of the presence of precipitates and elemental segregation at grain boundaries. However, in case of the model Fe-20Cr-XNi (X = 20, 30) alloys, the concentration of potential precipitate-forming elements such as C, N and S was < 0.005 wt%, and the approach to halve the activation energy for volume diffusion is justified. In the present work, a value of 25 μm (based on

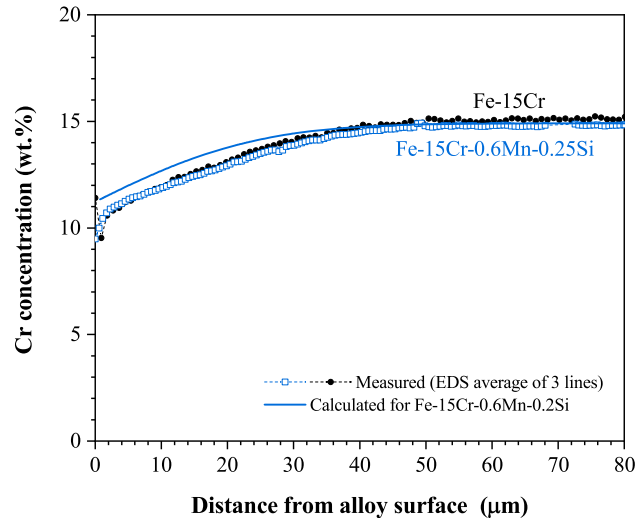


Fig. 4. Comparison between the measured (EDS) in Fe-15Cr and Fe-15Cr-0.6Mn-0.25Si after exposure for 100 h in the binary KCl-MgCl₂ eutectic (68:32 mol%) salt mixture at 800 °C. The solid line corresponds to the calculated Cr depletion profile for Fe-15Cr-0.6Mn-0.25Si at the same condition. The symbols correspond to the average Cr concentrations calculated from three measured concentration profiles across the specimen. No significant variation was observed between these measurements and the error bars spanning the minimum and maximum measured Cr concentrations from these measurements have been omitted for better readability. The solid line corresponds to the calculated Cr depletion profiles.

measured grain sizes) for d and 0.5 nm for δ , which is a typical grain boundary width in metallic materials, was used in Eq. 2 in the calculations. The activation energy for volume diffusion was extracted from the temperature dependence of the mobilities in the mobility database (MOBFE6).⁴²

Figure 6 compares the measured (EDS) and calculated Cr concentration profiles in the Fe-20Cr-20Ni (Fig. 6a) and Fe-20Cr-30Ni (Fig. 6b) model alloys after exposure for 100 h in the binary KCl-MgCl₂ eutectic (68:32 mol%) salt mixture at 800 °C in quartz capsules. The error bars spanning the minimum and maximum measured values of Cr concentrations demonstrate the variability in Cr depletion due to the microstructure-dependent transport across the specimen. The model was able to capture the observed Cr depletion in both model alloys with the approximated transport along the grain boundaries in the 1D model. In the case of Fe20Cr30Ni, the model underestimated the Cr depletion closer to the alloy surface but this can probably be attributed to the assumption of a constant grain size across the specimens and not accounting for local variations.

Multicomponent Alloys

To further verify the proposed hypotheses about the critical role of Cr activity in the alloy to govern corrosion rates, the Cr depletion was modeled in two commercial alloys, 230 and 740H (Table I). Alloy 230 is a solid solution-strengthened material with inter- and intragranular carbides (W, Mo and Cr-rich) while 740H is a precipitation strengthened material with about 20 vol% γ' at 760 °C. The calculated Cr activities (with BCC as reference state for Cr) of the commercial alloys 740H and 230 are higher than the model Fe-based alloys (Fig. 2b). The role of alloying additions on the Cr activity of 230 has been reported in the literature.^{18,45} The high W content in 230 results in a comparable Cr activity to

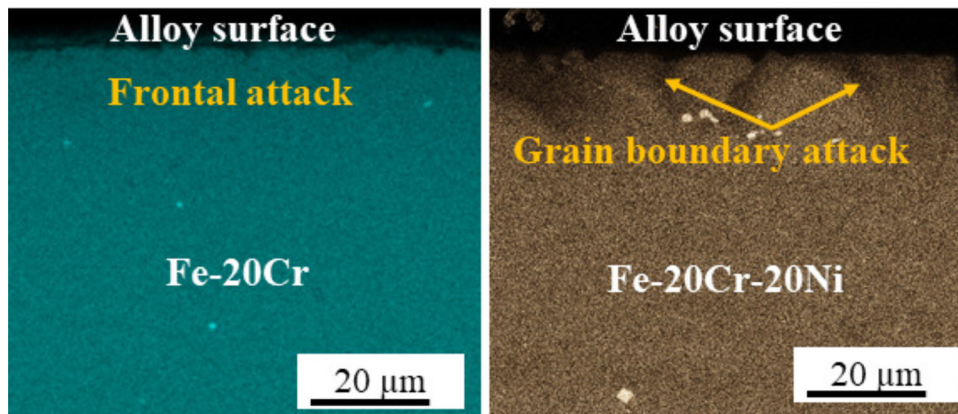
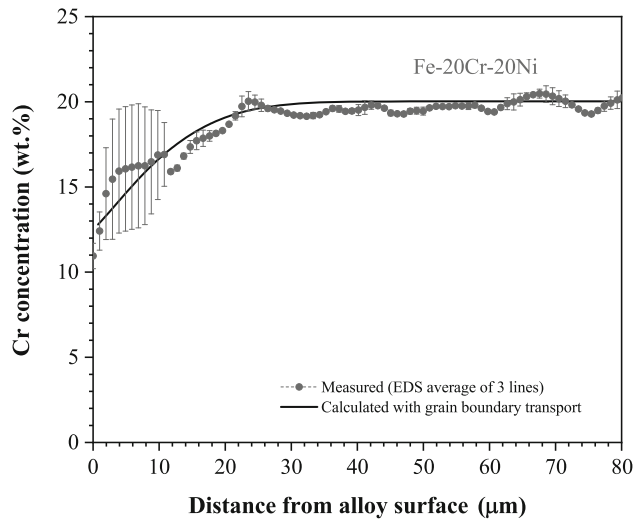
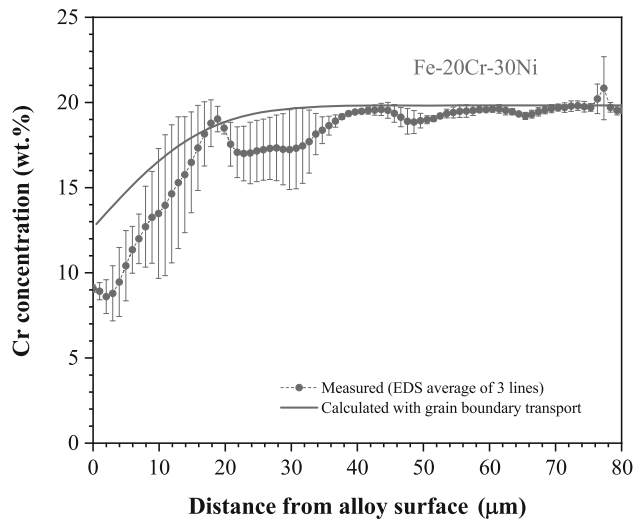


Fig. 5. Elemental distribution maps (EDS) for Cr in Fe-15Cr and Fe-20Cr-20Ni after exposure for 100 h in the binary KCl-MgCl₂ eutectic (68:32 mol%) salt mixture at 800 °C.



(a)

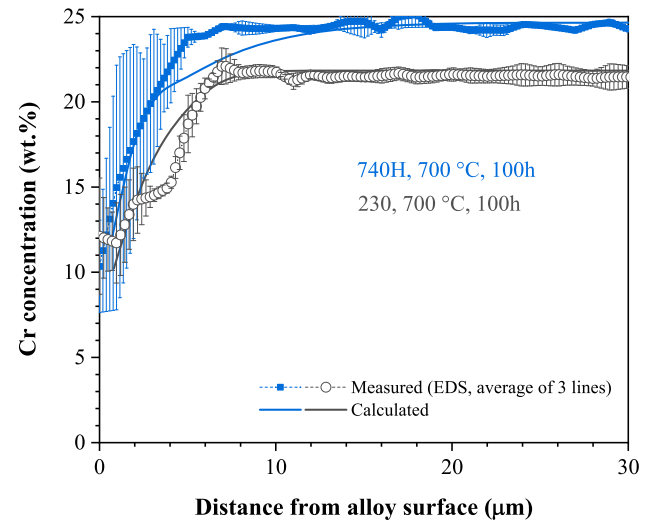


(b)

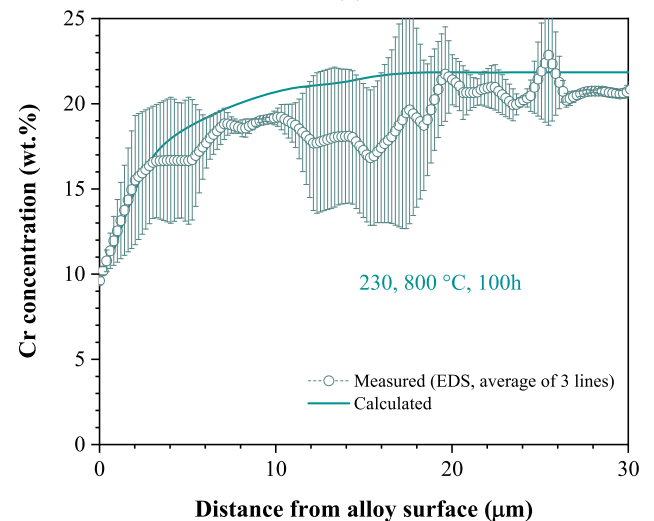
Fig. 6. Comparison between the measured (EDS) and calculated Cr concentration profiles in the (a) Fe-20Cr-20Ni and (b) Fe-20Cr-30Ni model alloys after exposure for 100 h in the binary KCl-MgCl₂ eutectic (68:32 mol%) salt mixture at 800 °C in quartz capsules.

740H at both temperatures although 230 has less Cr than 740H (Table I).

In case of the commercial alloys, a value of 50 μm (average value based on measured grain sizes) for d and 0.5 nm for δ was used to estimate the grain boundary mobility (Eq. 2). Similar to the model Fe-based alloys, the activation energy for grain boundary diffusion was taken as half of the value for volume diffusion. Figure 7a compares the measured and calculated Cr concentration profiles for alloys 740H and 230 after exposure for 100 h in the binary KCl-MgCl₂ eutectic (68:32 mol%) salt mixture at 700 °C. Except for slight local deviations, the model was generally able to predict the Cr depletion at 700 °C in both commercial alloys as the comparison in Fig. 7a shows. Additionally, the predicted Cr depletion in 230 after exposure for 100 h in the binary KCl-MgCl₂ eutectic (68:32 mol%) salt



(a)



(b)

Fig. 7. Comparison between the measured (EDS) and calculated Cr depletion profiles in alloys (a) 740H and 230 at 700 °C and (b) in 230 at 800 °C after exposure for 100 h in the binary KCl-MgCl₂ eutectic (68:32 mol%) salt mixture. The symbols correspond to the average Cr concentrations calculated from three measured concentration profiles across the specimen and the error bars span the minimum and maximum measured Cr concentrations from these measurements. The solid line corresponds to the calculated Cr depletion profiles.

mixture at 800 °C was in good agreement with the measured values (Fig. 7b).

Thermodynamic calculations (TCNI11) show that Cr activities in 740H (0.79) and 230 (0.8) are comparable at 700 °C (Fig. 2b). Based on the use of Eq. 5, this suggests that a similar Cr loss can be expected for 740H and 230 under the assumption of sole depletion of Cr from the alloys. Indeed, the depth of Cr depletion in the two alloys is very similar ($5 \mu\text{m} \pm 1 \mu\text{m}$ for 740H and $8 \mu\text{m} \pm 2 \mu\text{m}$ for 230). It must be noted though that these are short-term tests and larger differences between the corrosion behavior of these alloys can

be expected after longer exposure times. As emphasized in an earlier work by the authors,¹⁸ Cr depletion is additionally influenced by the corrosion-induced changes in chemical potentials (activities) and phase transformations during high temperature exposures.

Figure 8a shows the comparison between the measured (EDS) and calculated Al and Ti concentration profiles in 740H after exposure for 100 h in the binary KCl-MgCl₂ eutectic (68:32 mol%) salt mixture at 700 °C. Simultaneous enrichment of Al and Ti is predicted by the model driven by the corrosion-induced depletion of Cr. The measured concentration profiles do show enrichment but the model clearly is overestimating the enrichment of Ti. A few reasons for this might be local microstructural effects which the 1D model cannot capture, and the assumption of sole dissolution of Cr in the salt. Small amounts of Al (0.3 ppm) and Ti (0.5 ppm) were measured in the salts post-exposure suggesting concurrent dissolution of these elements in the salt, which will influence the chemical interactions between the alloying constituents and thereby the consequent compositional changes and phase transformations. The dissolution of alloying constituents other than Cr in molten halide salts has been reported before and will strongly depend on temperature, salt chemistry and alloy composition. Simultaneous dissolution of Fe and Cr was observed in the Ni-based commercial alloy IN600 during exposures in molten chloride salt at 600 °C and 650 °C while only Cr was observed to be depleted at 700 °C.¹⁸ Raiman et al.⁴⁶ observed deposition of primarily Fe on the cold leg (540 °C) specimens exposed to flowing FLiNaK salt for 1000 h in a monometallic material thermal convection loop (TCL) corresponding to the simultaneous dissolution of Fe and Cr from the hot leg (maximum temperature of 650 °C) specimens. In case of 740H, Al and Ti both serve as γ' stabilizers, and thermodynamic equilibrium calculations with the measured increase in their compositions on the surface of 740H suggest an increase in the γ' fraction. Diffusion in γ' is known to be slower, which will change the diffusion kinetics of the alloying constituents near the surface. Since the model does not consider Al and Ti dissolution, it overestimates the enrichment of Al and Ti and hence the fraction of γ' on the surface. This is probably an additional reason for the observed deviations between measurements and model predictions closer to the surface.

The role of W in governing molten salt-induced corrosion of 230 by increasing the Cr activity was discussed in a previous work by the authors.¹⁸ A similar finding was also reported by Liu et al. for ternary Ni-Cr-W alloys exposed in molten FLiNaK salt at 850 °C.⁴⁷ Figure 8b compares the measured and calculated W concentration profiles in 230 after exposure for 100 h in the binary KCl-MgCl₂ eutectic (68:32 mol%) salt mixture at 700 °C. The enrichment of W in the alloy subsurface is accurately

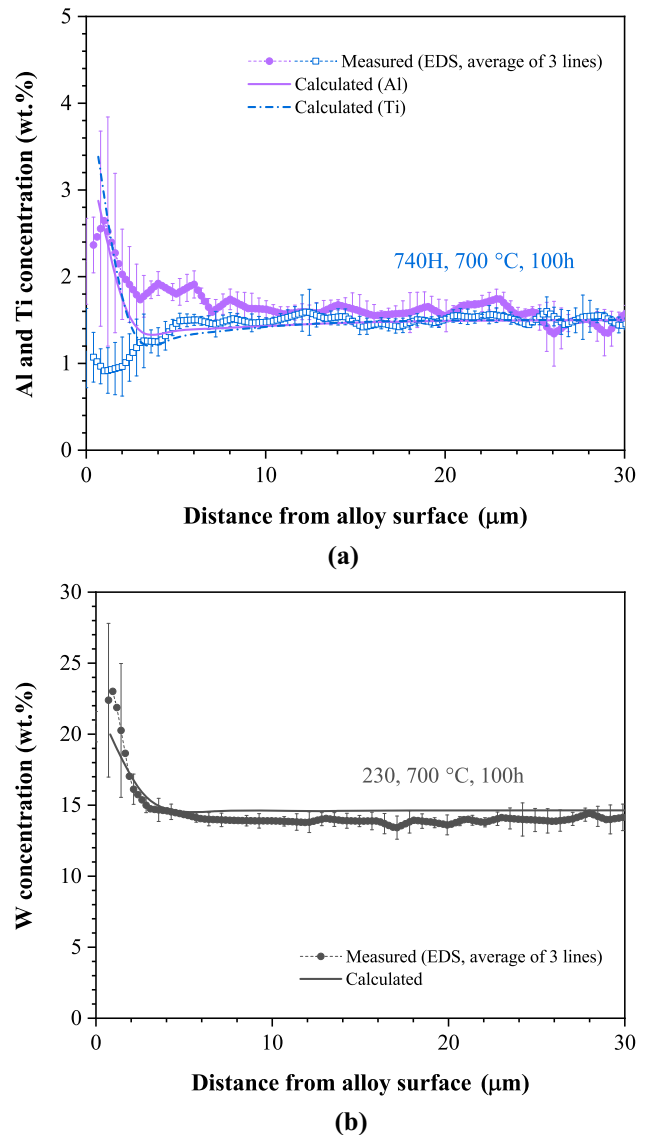


Fig. 8. Comparison between the measured (EDS) and calculated Cr depletion profiles in alloys (a) 740H and 230 at 700 °C and (b) in 230 at 800 °C after exposure for 100 h in the binary KCl-MgCl₂ eutectic (68:32 mol%) salt mixture. The symbols correspond to the average Cr concentrations calculated from three measured concentration profiles across the specimen, and the error bars span the minimum and maximum measured Cr concentrations from these measurements. The solid line corresponds to the calculated Cr depletion profiles.

predicted by the model. An increase in the W concentration at the surface will increase the surface Cr activity and sustain the Cr dissolution rate (Eq. 5). A comparison of the temporal evolution of the surface Cr activities in 230 and 740H during exposure for 100 h in the binary KCl-MgCl₂ eutectic (68:32 mol%) salt mixture at 700 °C is shown in Fig. 9. The surface Cr activity was predicted to drop by 40% within the first few hours for 740H, while in the case of 230, it remains constant up to almost 10 h. A considerably slower drop in surface Cr activity is evident for 230 compared to 740H

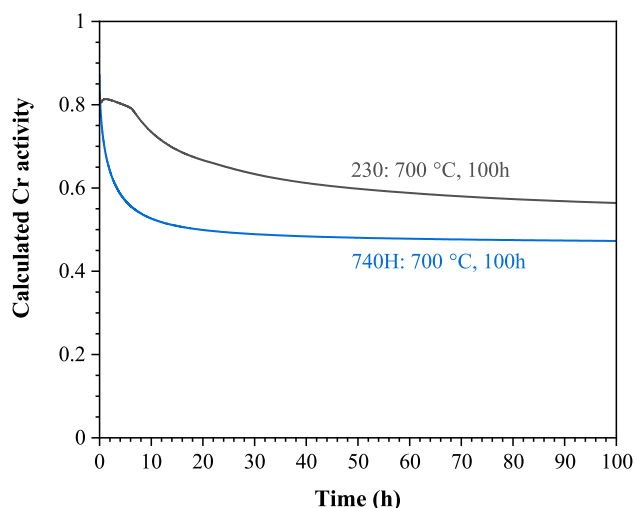


Fig. 9. Calculated (TCNI11) Cr activity on the alloy surface in 230 and 740H during exposure for 100 h in the binary KCl-MgCl₂ eutectic (68:32 mol%) salt mixture at 700 °C.

during the total exposure duration of 100 h, which will be expected to continue to drive Cr dissolution (Eq. 5). Moreover, depletion of Cr has been shown to result in the dissolution of carbides in the subsurface of 230 after exposure in molten chloride salt for 92 h at 800 °C.¹⁸ Dissolution of carbides can provide newer sites for continued attack in 230, which might explain the strong depletion of Cr in the grain boundaries of 230 at 800 °C indicated by the concentration profile (Fig. 7).

Additional Validation of the Modeling Approach

The predictive capability of the model for longer exposure times was evaluated by comparing the calculated and measured Cr depletion in the Fe-20Cr specimen exposed for 2000 h at 800 °C in a quartz capsule (Fig. 10). Although further comparison with long-term exposures of a wide range of alloy compositions is essential, the accurate simulation of the observed Cr depletion behavior in the binary Fe-20Cr alloy validates the modeling approach presented here. Furthermore, the assumptions of scaling the Cr dissolution rates in multicomponent alloys with the measured rates of pure Cr and assigning corresponding power law kinetics are justified in this case. It must be noted that the measured Cr concentrations on the alloy surface are similar (15.5 wt%) in the Fe-20Cr specimens exposed in the binary KCl-MgCl₂ eutectic (68:32 mol%) salt mixture for 100 h (Fig. 3a) and 2000 h (Fig. 10) but the depth of Cr depletion is much deeper after 2000 h (250 μm) than after 100 h (50 μm). A surface concentration independent of time is further evidence of parabolic corrosion kinetics.⁴⁸

The area-specific Cr loss (g cm⁻²) from the model predictions was estimated by integrating the area under the calculated concentration profiles and

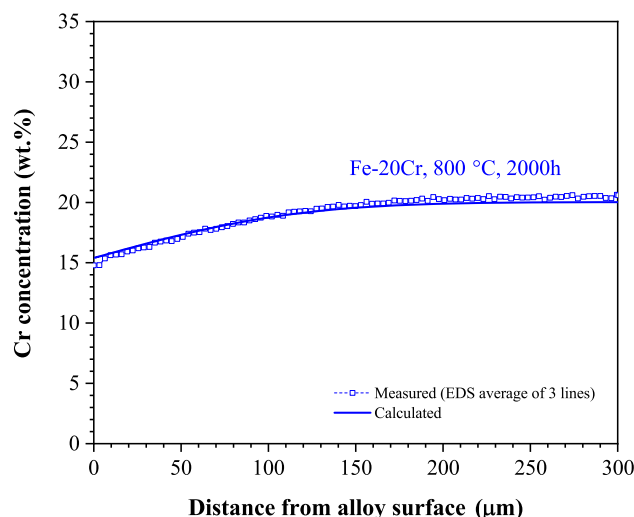


Fig. 10. Comparison between the measured (EDS) and calculated Cr concentration profiles in Fe-20Cr (wt%) after exposure for 2000 h in the binary KCl-MgCl₂ eutectic (68:32 mol%) salt mixture at 800 °C in quartz capsules.

multiplying with the alloy density (assuming 8 g cm⁻³ for the model alloys and 740 H while 9 g cm⁻³ for 230). The amount of Cr (g) dissolved in the salt can then be estimated with the surface area of the specimens. Figure 11 compares the measured Cr content in the salts with the predicted Cr loss after exposure for 100 h in the binary KCl-MgCl₂ eutectic (68:32 mol%) salt mixture at 700 °C (Fig. 11a) and 800 °C (Fig. 11b). It is evident from the figures that the model was well able to predict the time, temperature and alloy composition dependent dissolution of Cr in the binary KCl-MgCl₂ salt. Predominant dissolution of Cr was confirmed with the measurements of the salt chemistry after exposure with the highest measured contents of Cr compared to other alloying constituents. An exception was the Fe-based alloys in which the highest measured Fe content in the salt corresponded to the Fe-15Cr specimen and was 13.8 ppm after exposure for 100 h at 700 °C but it dropped to 4 ppm at 800 °C. The model did not consider dissolution of Fe, which might have resulted in underestimation of the Cr dissolution at 700 °C and 800 °C for the Fe-15Cr specimen 700 °C. Minor amounts (maximum 4 ppm) of Mn, Si and Ni were measured in the respective model alloys (Fe15CrMnSi, Fe20Cr20Ni, Fe20Cr30Ni). As mentioned in the previous section, minor amounts of Al and Ti were measured in the salt corresponding to the 230 specimen at 700 °C and 800 °C.

The results shown in the current work are encouraging since they validate the hypothesis presented in an earlier work by the authors¹⁸ and reiterate that simultaneous consideration of thermodynamics (chemical activities) and kinetics (transport in the alloys) can adequately describe the observed corrosion behavior of multicomponent structural materials during static isothermal testing in purified molten salts. The combined

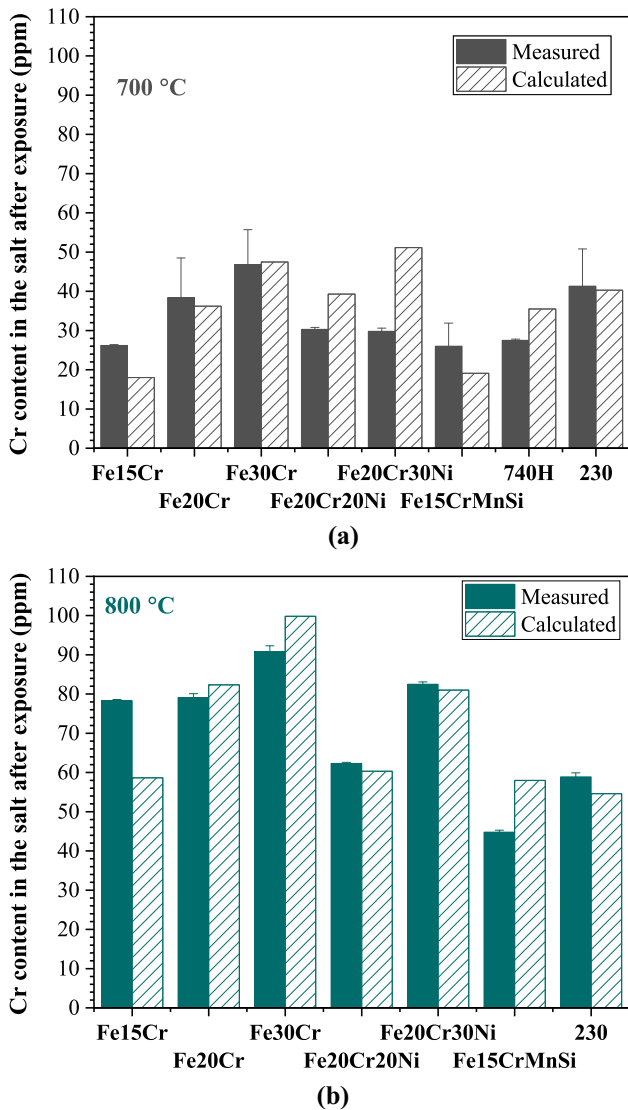


Fig. 11. Measured Cr content in the salt after exposure for 100 h in the binary KCl-MgCl₂ eutectic (68:32 mol%) salt mixture at (a) 700 °C and (b) 800 °C compared with the calculated Cr loss from the alloys under the same conditions.

experimental-computational approach presented here opens a new path for establishing alloy design strategies for structural materials envisioned to operate in molten salt technologies under yet untested operating conditions.

CONCLUSION

The current work was successful in validating the hypothesis presented in a previous work by the authors emphasizing the role of chemical potential gradients in the alloy in driving molten salt corrosion. The Cr corrosion rates from multicomponent Fe-based and Ni-based alloys during exposure in high-purity binary KCl-MgCl₂ salt were derived from corresponding exposures of pure Cr in the same salt at 700 °C and 800 °C. The predicted microstructural evolution (element distribution and

compositional changes) in the alloys during corrosion was in very good agreement with experimental observations suggesting an accurate description of underlying mechanisms. Based on the results, it can be concluded that an alloy with a higher initial Cr activity will most likely tend to corrode more under similar conditions (temperature, salt chemistry, capsule material) but subsequent transport processes will govern the long-term corrosion behavior. This was shown for the case of 230 where selective depletion of Cr resulted in a subsurface enrichment of W that increased and thereby negated the drop in the surface Cr activity due to its corrosion-induced depletion and supported continued dissolution of Cr.

The methodology presented here to quantify corrosion rates and predict microstructural evolution of metallic materials during exposures in molten chloride salts can be employed as a template for application-specific design of structural materials for molten salts. The results of the current work also emphasize the value of generating data on the time-, temperature- and salt chemistry-dependent dissolution of pure elements in a wide range of practically relevant salt chemistries (chlorides and fluorides). Relevant data for dissolution of Cr and Fe in molten chloride and fluoride salts are currently being generated as part of ongoing studies. With this information, dissolution of multiple alloying constituents can be integrated into the thermodynamic-kinetic model for prediction of their concurrent depletion. Ultimately, this tool can be coupled with models predicting thermodynamics of salt-alloy systems and high-dimensionality models (e.g., phase field models) to accurately describe the composition, temperature and microstructure dependence of the multidimensional transport processes in the alloys and enable a more realistic representation of material behavior under in-service conditions of molten salts technologies.

ACKNOWLEDGEMENTS

A. Willoughby assisted with the experimental work at ORNL. V. Cox is thanked for helping with metallography and microstructural characterization respectively. J. Keiser and M. Romedenne are thanked for their valuable comments on the paper. This research was sponsored by the US Department of Energy Office of Nuclear Energy, Molten Salt Reactor Campaign and the Nuclear Energy Advanced Modeling and Simulation program.

CONFLICT OF INTEREST

The authors declare that they have no conflict of interest.

REFERENCES

1. C. Le Brun, *J. Nucl. Mater.* **360**(1), 1 (2007). <https://doi.org/10.1016/j.jnucmat.2006.08.017>.

2. G. Locatelli, M. Mancini, N. Todeschini, *Energy Policy* **61**, 1503 (2013). <https://doi.org/10.1016/j.enpol.2013.06.101>.
3. J. Serp, M. Allibert, O. Benes, S. Delpech, O. Feynberg, V. Ghetta, D. Heuer, D. Holcomb, V. Ignatiev, J.L. Kloosterman, L. Luzzi, E. Merle-Lucotte, J. Uhler, R. Yoshioka, Z.M. Dai, *Progr. Nucl. Energy* **77**, 308 (2014). <https://doi.org/10.1016/j.pnucene.2014.02.014>.
4. A. Tonti, C. Renault, M. Sperandio, C. DelleSite, G. Baylac, F. Carre, *Proc. Asme Pressure Vessels Piping Conf.* **1**, 657 (2009).
5. M. Mehos, C. Turchi, J. Vidal, M. Wagner, Z. Ma, C. Ho, W. Kolb, C. Andracka, A. Kruiuzenga, *Concentrating Solar Power Gen3 Demonstration Roadmap*, Report NREL/TP-5500-67464, NREL, (2017).
6. C.W. Forsberg, *Int. J. Hyd. Energy* **28**(10), 1073 (2003).
7. P.N. Haubenreich, *Nucl. Eng. Int.* **14**(155), 325 (1969).
8. M.W. Rosenthal, P.R. Kasten, R.B. Briggs, *Nucl. Appl. Technol.* **8**(2), 107 (1970). <https://doi.org/10.13182/Nt70-A28619>.
9. W. Manly, G. J. Adamson, J. Coobs, J. DeVan, D. Douglas, E. Hoffman, P. Patriarca, *Aircraft Reactor Experiment—Metallurgical Aspects*, Report ORNL-2349 United States 10.2172/4227617 NTIS ORNL English, ; Oak Ridge National Lab., Tenn., <https://www.osti.gov/servlets/purl/4227617>, other Information: Decl. Oct. 9, 1959. Orig. Receipt Date: 31-DEC-60, (1958).
10. J.C. Gomez-Vidal, R. Tirawat, *Solar Energy Mater. Solar Cells* **157**, 234 (2016). <https://doi.org/10.1016/j.solmat.2016.05.052>.
11. G.Q. Zheng, K. Sridharan, *Jom* **70**(8), 1535 (2018). <https://doi.org/10.1007/s11837-018-2981-2>.
12. H. Sun, J.Q. Wang, Z.J. Li, P. Zhang, X.Z. Su, *Solar Energy* **171**, 320 (2018). <https://doi.org/10.1016/j.solener.2018.06.094>.
13. B.A. Pint, J.W. McMurray, A.W. Willoughby, J.M. Kurley, S.R. Pearson, M.J. Lance, D.N. Leonard, H.M. Meyer, J. Jun, S.S. Raiman, R.T. Mayescirc, *Mater. Corros.* **70**(8), 1439 (2019). <https://doi.org/10.1002/maco.201810638>.
14. J. H. De Van Thesis ORNL/TM-2021/1, (1969).
15. I.N. Ozeryanaya, *Metal Sci. Heat Treat.* **27**(3), 184 (1985). <https://doi.org/10.1007/bf00699649>.
16. A. Kruiuzenga, *Corrosion Mechanisms in Chloride and Carbonate Salts*, Report SAND2012-7594, Sandia National Laboratories, (2012).
17. W. Ding, H. Shi, Y. Xiu, A. Bonk, A. Weisenburger, A. Jianu, T. Bauer, *Solar Energy Mater. Solar Cells* **184**, 22 (2018). <https://doi.org/10.1016/j.solmat.2018.04.025>.
18. R. Pillai, S.S. Raiman, B.A. Pint, *J. Nucl. Mater.* (2021). <https://doi.org/10.1016/j.jnucmat.2020.152755>.
19. H.S. Cho, J.W. Van Zee, S. Shimpalee, B.A. Tavakoli, J.W. Weidner, B.L. Garcia-Diaz, M.J. Martinez-Rodriguez, L. Olson, J. Gray, *Corrosion* **72**(6), 742 (2016). <https://doi.org/10.5006/1865>.
20. B.A.T. Mehrabadi, J.W. Weidner, B. Garcia-Diaz, M. Martinez-Rodriguez, L. Olson, S. Shimpalee, *J. Electrochem. Soc.* **163**(14), C830 (2016). <https://doi.org/10.1149/2.0411614jes>.
21. J. H. DeVan, R. B. Evans, III, *Corrosion Behavior of Reactor Materials in Fluoride Salt Mixtures*, Report ORNL-TM-328, <https://doi.org/10.2172/4774669>, (1962).
22. H.E. McCoy, R.L. Beatty, W.H. Cook, R.E. Gehlbach, C.R. Kennedy, J.W. Koger, A.P. Litman, C.E. Sessions, J.R. Weir, *Nucl. Appl. Technol.* **8**(2), 156 (1970). <https://doi.org/10.13182/Nt70-A28622>.
23. G. Zheng, L. He, D. Carpenter, K. Sridharan, *J. Nucl. Mater.* **482**, 147 (2016). <https://doi.org/10.1016/j.jnucmat.2016.10.023>.
24. C. Falconer, W.H. Doniger, L. Bailly-Salins, E. Buxton, M. Elbakshwan, K. Sridharan, A. Couet, *Corros. Sci.* **177**, 108955 (2020). <https://doi.org/10.1016/j.corsci.2020.108955>.
25. C. Falconer, M. Elbakshwan, W. Doniger, M. Weinstein, K. Sridharan, A. Couet, *npj Mater. Degrad.* **6**(1), 29 (2022). <https://doi.org/10.1038/s41529-022-00239-z>.
26. S. S. Raiman, J. W. McMurray, R. T. Mayes, C. Abney, K. Myhre, J. R. Keiser, B. R. Betzler, T. Muth, D. Sulejmanovic, *Fundamental Studies of Materials Degradation in Molten Chloride Salts Using Targeted Corrosion Testing, Advanced Spectroscopy, and Thermodynamic Modeling*, unpublished work (2019).
27. R. Pillai, W. Sloof, A. Chyrkin, L. Singheiser, W. Quadackers, *Mater. High Temp.* **32**, 57 (2015).
28. G.S. Chen, I.W. Sun, K.D. Sienerth, A.G. Edwards, G. Mamantov, *J. Electrochem. Soc.* **140**(6), 1523 (1993). <https://doi.org/10.1149/1.2221596>.
29. R. T. Mayes, J. M. Kurley III, P. W. Halstenberg, A. McAlister, D. Sulejmanovic, S. S. Raiman, S. Dai, B. A. Pint, *Purification of Chloride Salts for Concentrated Solar Applications*, Report ORNL/LTR-2018/1052, (2018).
30. H. Larsson, A. Engström, *Acta Materi.* **54**(9), 2431 (2006). <https://doi.org/10.1016/j.actamat.2006.01.020>.
31. A. Chyrkin, R. Pillai, H. Ackermann, H. Hattendorf, S. Richter, W. Nowak, D. Grüner, W. Quadackers, *Corros. Sci.* **96**, 32 (2015). <https://doi.org/10.1016/j.corsci.2015.03.019>.
32. A. Chyrkin, W. Sloof, R. Pillai, T. Galiullin, D. Grüner, W. Quadackers, *Mater. High Temp.* **32**, 102 (2015).
33. R. Pillai, A. Chyrkin, T. Galiullin, E. Wessel, D. Gruener, W.J. Quadackers, *Corros. Sci.* **127**, 27 (2017). <https://doi.org/10.1016/j.corsci.2017.07.021>.
34. T.J. Nijdam, W.G. Sloof, *Acta Mater.* **56**(18), 4972 (2008). <https://doi.org/10.1016/j.actamat.2008.06.010>.
35. K. Yuan, R. Eriksson, R.L. Peng, X.-H. Li, S. Johansson, Y.-D. Wang, *Surf. Coat. Technol.* **232**, 204 (2013). <https://doi.org/10.1016/j.surfcoat.2013.05.008>.
36. R. Pillai, M.P. Taylor, T. Galiullin, A. Chyrkin, E. Wessel, H. Evans, W.J. Quadackers, *Mater. High Temp.* **35**(1–3), 78 (2018).
37. R. Pillai, E. Wessel, W.J. Nowak, D. Naumenko, W.J. Quadackers, *Jom* **70**(8), 1520 (2018).
38. H. Larsson, H. Strandlund, M. Hillert, *Acta Mater.* **54**, 945 (2006).
39. Thermo-Calc, TCFE11, TCS Fe-based Alloys Database, v11.0, 2020, (2020).
40. Thermo-Calc, TCNI11, TCS Ni-based superalloys Database, v11.0, 2021, (2021).
41. Thermo-Calc, MOBNI5, TCS Ni-alloys Mobility Database, v5.1, 2019, (2019).
42. Thermo-Calc, MOBFE, TCS Steel Mobility Database, v6.0, 2020, (2020).
43. Z. Tokei, H. Viefhaus, K. Hennesen, H.J. Grabke, *Diff. React.* **72**, 3 (2000). <https://doi.org/10.4028/www.scientific.net/SSP.72.3>.
44. P. Shewmon, *Diffusion in Solids*, 2nd edn. (Springer, Cham, 2016). <https://doi.org/10.1007/978-3-319-48206-4>.
45. A. Jalowicka, R. Duan, P. Huczukowski, A. Chyrkin, D. Gruner, B.A. Pint, K.A. Unocic, W.J. Quadackers, *Jom* **67**(11), 2573 (2015).
46. S.S. Raiman, J.M. Kurley, D. Sulejmanovic, A. Willoughby, S. Nelson, K. Mao, C.M. Parish, M.S. Greenwood, B.A. Pint, *J. Nucl. Mater.* **561**, 153551 (2022). <https://doi.org/10.1016/j.jnucmat.2022.153551>.
47. S. Liu, X.-X. Ye, S. Yan, X. Wang, B. Leng, X. Zhou, *Corros. Sci.* **191**, 109761 (2021). <https://doi.org/10.1016/j.corsci.2021.109761>.
48. R. Pillai, H. Ackermann, K. Lucka, *Corros. Sci.* **69**, 181 (2013). <https://doi.org/10.1016/j.corsci.2012.11.040>.

Publisher's Note Springer Nature remains neutral with regard to jurisdictional claims in published maps and institutional affiliations.

Springer Nature or its licensor (e.g. a society or other partner) holds exclusive rights to this article under a publishing agreement with the author(s) or other rightsholder(s); author self-archiving of the accepted manuscript version of this article is solely governed by the terms of such publishing agreement and applicable law.